THE ASTRONOMICAL JOURNAL VOLUME 89, NUMBER 4 APRIL 1984

COMA MORPHOLOGY AND DUST-EMISSION PATTERN OF PERIODIC COMET HALLEY. I. HIGH-RESOLUTION IMAGES TAKEN AT MOUNT WILSON IN 1910

S. M. LARSON
Lunar and Planetary Laboratory, University of Arizona, Tucson, Arizona 85721

Z. SEKANINA
Jet Propulsion Laboratory, California Institute of Technology, Pasadena, California 91109
Received 19 December 1983

ABSTRACT

A new image-processing algorithm has been devised to improve visibility of features in the head of Comet Halley on the high-resolution photographs taken at Mount Wilson in May–June 1910. The most striking features are spiral jets that "unwind" from the central condensation and evolve into expanding envelopes on a time scale of days. They consist of dust particles ejected continuously from discrete regions on the sunlit side of the rotating nucleus and are, in their early phase of development, essentially two-dimensional formations. We find ~ 1 day as a crude lower limit to the comet's rotation period. The projected expansion velocities of the dust features are measured to range from 0.2 to 0.3 km/s. Relative photometry of a bright jet suggests that the column density of dust ejecta in the jet exceeds the density in the coma by a factor of $\gtrsim 2$ and that, if narrow along the line of sight, the jet may have a particle number concentration several tens of times higher than the coma background. Numerous ion features are also seen on the photographs. The 1910 images give a preview of the type of activity that the Near-Nucleus Studies Network of the International Halley Watch will be concerned with during Comet Halley's upcoming apparition. The developed image-processing capability will be indispensable for the reduction of the observations.

I. INTRODUCTION

Many brighter comets, including Periodic Comet Halley, show coma structure that changes from night to night (cf. Rahe, Donn, and Wurm 1969). The features, which include jets, fans, arcs, and halos, are products of directed emission of material and serve as evidence of a nonuniform surface structure of the cometary nucleus. Visual telescopic observations emphasize the boundaries of changing intensity gradients and make the usually low-contrast coma features look more prominent than they in fact are. In general, the visibility of these features depends upon aperture, magnification, and also sky brightness and transparency. Together with varying competency of the visual observers these conditions are responsible, on numerous occasions, for an embarrassing lack of resemblance among drawings obtained virtually at the same time (cf. various sets of visual observations in Rahe, Donn, and Wurm 1969). With rare exceptions, quantitative analysis of drawings is not possible.

Photographic observations of coma structure are free from many pitfalls of visual observation, but have problems of their own. A useful photograph must have a high spatial resolution, a correct exposure time, precise guiding on the comet, and must be obtained in good seeing. The choices of emulsion and filter as well as the photographic processing also affect the quality of the result. Finally, a successful positional reduction and analysis require that the features be visible in the eyepiece of the measuring machine under magnification that reduces the contrast. Only recently has this last problem been alleviated by the digital image processing of the photographs and the situation further improved by the introduction, at the telescope, of highly sensitive solid-state detector arrays, such as charge-coupled devices.

Interest in high-resolution coma imaging has increased considerably after it was demonstrated quantitatively that the structure of the dust coma contains information on the spin vector and can even be used to pinpoint the regions of unusually high dust production on the nucleus surface (Larson and Minton 1972; Larson 1978; Whipple 1978, 1980, 1982; Sekanina 1979, 1981a,b).

II. PHOTOGRAPHS OF COMET HALLEY

Although photographic emulsions were relatively insensitive in 1910, quality images of Comet Halley at high spatial resolution were obtained with two large reflectors—the 152-cm $f/5$ at Mount Wilson and the Crossley 91-cm $f/5.8$ at Mount Hamilton. Useful photographs of lower resolution were also obtained with smaller reflectors and with astrographs of long focal length, especially during the time of the comet's peak brightness in May and June 1910. Complete information on the world-wide photographic observations of the comet has never been published, but extensive lists were prepared by Comstock *et al.* (1915) and by Bobrovnikoff (1931).

In this first of a series of papers that we intend to write on coma structure of P/Halley, we utilize the images obtained by G. W. Ritchey with the 152-cm reflector at Mount Wilson. These well-preserved photographs have a plate scale of about 27 arcsec per millimeter. The periods of observation were May 5–11 and June 2–6, 1910. The exposure times varied from 1.5 to 25 min. The shorter exposures are better for near-nucleus detail, whereas the longer exposures give a better signal-to-noise ratio for faint, outer envelopes. With one exception (a 90-s exposure on May 7.5 UT), the emulsions used were Seed 23 and 27.

A total of 31 plates were taken on the 12 nights. After their digitization we selected the best single plate each night for further study. The precise scale and orientation of each plate were determined from positional measurement of field stars and the position of the point of maximum photographic density was tested relative to the comet's topocentric path calculated from the best available orbital elements (Yeomans 1983, private communication). Deviations of the observed center of light from the ephemeris position corresponding to the recorded time of observation were given as the residuals along and across the comet's track, $\Delta\psi$ and $\Delta\epsilon$. As shown below, these residuals are mostly very small, especially in the direction normal to the motion. Since the times of observation were recorded with rather low precision (usually rounded off to the nearest minute, not compared with a time standard), we attributed the residuals $\Delta\psi$ to uncertainties in the times and applied corrections $\Delta t = \Delta\psi/\dot{s}_{\rm mot}$, where $\dot{s}_{\rm mot}$ is the comet's apparent motion. The exposures appear to have been guided in one axis after the edge of the longer side of each 12×9 cm plate had been aligned approximately with the comet's expected direction of motion.

The 12 selected plates are listed in Table I which gives: the time of mid-exposure, corrected for the contribution from $\Delta\psi$; the geocentric and heliocentric distances, Δ and r; the position angle of the prolonged radius vector, $P_{\rm RV}$; the apparent rate and position angle of the comet's topocentric motion, $\dot{s}_{\rm mot}$ and $P_{\rm mot}$ (not including differential refraction); the measured position angle of the edge of the plate's longer side, $P_{\rm edge}$; the measured plate scale; the residuals $\Delta\psi$ (measuring the applied correction to the original time of observation and reckoned positive ahead of the ephemeris place) and $\Delta\epsilon$ (positive to the north of the comet's path); the plate emulsion used; and the specified exposure time.

III. IMAGE PROCESSING

The coma features on the Mount Wilson photographs are almost always of low contrast and superimposed on an intensity gradient of long dynamic range. In general, the feature contrast appears to diminish with increasing distance from the nucleus. These conditions require use of digital image-processing techniques to enhance the contrast.

Various approaches to image enhancement have been applied to comets (e.g., Klinglesmith 1981; Matuska *et al.* 1978; Sekanina and Farrell 1978; Wood and Albrecht 1981). The most common techniques utilize spatial filtering or take intensity derivatives in some direction. These methods reduce the effects of the steep intensity falloff and allow one to stretch the contrast. In all of these approaches, great care must be exercised to identify processing artifacts that may be misleading in the analysis. One of the most successful methods has been the linear intensity derivative using a linear shift-difference algorithm. The primary limitation of this technique is that it emphasizes only the features which have an intensity change in the direction of the shift. Figure 1 [Plate 11] shows the effect of a linear shift-difference process on an image; note the feature's strong visibility dependence on the direction of the shift.

According to Bobrovnikoff (1931), one characteristic property of P/Halley was a persistent appearance of nearly circular halos, centered approximately on the nucleus. It seems that a shift difference radial to the center of light should improve visibility of these features, as it maps the rate of change of emission at a given position angle. A severe limitation is that the features oriented radial to the nucleus, such as jets or ion streamers, do not show. To make these features visible, a rotational shift difference (about the center of light) must be applied. Figure 2 [Plate 12] shows the result of application of various amounts of radial and rotational shift differences. The rotational component tends to emphasize features of varying spatial extent depending upon the distance from the nucleus. This, however, is not a serious problem as features become larger and more diffuse farther from the nucleus and require a larger shift to show.

To ensure that features of any orientation are retained in the processing, we add two processed images which have the same radial shifts and the rotational shifts of the same magnitude but opposite directions. The relation between B and B', the brightnesses of an unprocessed and processed pixel, is

$$B'(x, P; \Delta x, \Delta P) = [B(x, P) - B(x - \Delta x, P - \Delta P)] + [B(x, P) - B(x - \Delta x, P + \Delta P)], \tag{1}$$

where x and P are the point's radial distance and position angle relative to the comet's maximum brightness, Δx is a radial and ΔP a rotational shift. The optimum parameters must be found empirically in each case. It is important to consult the original image to ensure that processing artifacts are not introduced and that the general appearance of the features is not distorted so as to mislead interpretation. The final images are maps of intensity changes with steep positive-gradient changes dark, negative-gradient changes light, and near-zero gradients (such as the sky) grey.

In this study the Kitt Peak National Observatory's PDS scanning microdensitometer was employed to digitize the original plates. Arrays of 500×500 elements with a pixel size of 40 microns (or ~ 1 arcsec) a side were used, since the available output was a standard 512×512-image display system. The point of maximum density in the coma was taken as the primary reference and the array was aligned with the plate edge. None of the plates had sensitometric calibra-

TABLE I. Mount Wilson plates of Comet Halley selected for analysis.

Time of mid-exposure 1910 (UT)		Δ (AU)	r (AU)	$P_{\rm RV}$	Apparent motion $\dot{s}_{\rm mot}$ (min^{-1})	Apparent motion $P_{\rm mot}$	$P_{\rm edge}$	Plate scale (mm^{-1})	Residuals $\Delta\psi$	Residuals $\Delta\epsilon$	Emulsion	Exposure time (min)
May	5.4900	0.63618	0.67534	255°.6	1″.65	70°.9	67°.8	27″.34	+1″.0	−1″.3	Seed 23	8
	6.4827	0.59701	0.68600	255.5	1.99	71.3	79.1	27.23	+0.3	+0.4	Seed 23	4
	7.4931	0.55719	0.69728	255.4	2.39	71.6	73.9	27.36	0.0	+0.1	Seed 23	4
	8.4885	0.51807	0.70879	255.3	2.87	72.0	74.8	27.32	+6.9	−0.1	Seed 23	8
	9.4875	0.47901	0.72071	255.3	3.47	72.3	74.7	27.20	+3.6	+2.5	Seed 23	8
	10.4938	0.43994	0.73306	255.3	4.23	72.6	74.2	27.15	−0.3	−0.9	Seed 23	2
	11.4932[a]	0.40156	0.74565	255.5	5.19	73.1	74.0	27.15	+7.7	...	Seed 23	2
June	2.1815	0.53143	1.06120	112.2	3.04	110.1	104.3	27.17	+13.2	+0.1	Seed 27	12
	3.2288	0.57117	1.07734	112.4	2.66	110.2	104.1	26.98	−1.5	−2.5	Seed 23	25
	4.2246	0.60901	1.09273	112.6	2.35	110.2	103.5	27.17	−2.5	+1.0	Seed 23	25
	5.2367	0.64750	1.10837	112.7	2.09	110.2	104.0	27.18	−2.4	+0.1	Seed 27	20
	6.2175	0.68478	1.12354	112.9	1.88	110.2	106.4	27.07	−1.9	−2.4	Seed 27	9

[a] Time corrected on the assumption of $\Delta\epsilon = 0$.

tion. Developing information and typical sensitometric response were unavailable as well, and some plates were later treated for "hypo stains," which altered the densities by some unknown amount. For these reasons nearly all of the images have been kept in their density configuration.

IV. DESCRIPTION OF THE FEATURES

The computer-enhanced structure of the comet's head, compared in Figs. 3–6 [Plates 13–16] with the unprocessed images, resembles drawings by visual observers. For uniformity, the processing parameters, $\Delta x = 5$ pixels, $\Delta P = 10°$, are identical for all the images.

A study of the coma morphology is complicated by the broad spectral bandpass of the emulsions used. Spectrograms of P/Halley (Bobrovnikoff 1931) show that the images consist primarily of the contributions from the usual molecular species, from scattered solar continuum, and from ion emissions. Identification of these components in the direct images can only be made using guidelines based on their recognized morphological characteristics in comets. We identify solids by their sunward asymmetry and by changes that imply subkilometer-per-second velocities. Because of chaotic molecular motions, gas emissions have a nearly symmetric distribution and lack discrete features. Ion emissions are identified by sharply defined structure which changes on very short time scales as a result of the interaction with the highly variable solar-wind magnetic field. They are especially strong in the June images.

The single most striking quality of the processed images in Figs. 3–6 is evidence of the constant formation of spiral jets that are seen to "unwind" from the central condensation on the sunward side of the coma. This spiral pattern is strongly indicative of a spinning nucleus. In particular, an apparent clockwise rotation on the May images and counterclockwise rotation on the June images are consistent with expectation, because the Earth-comet vector had turned by about 150° between May 7 and June 4, and the probability of the Earth's transit across the equatorial plane of a randomly oriented nucleus between the two dates is more than 90%.

A number of features in Figs. 3–6 can be followed over several days. We have already shown (Sekanina and Larson 1983) that the observed evolution of a spiral jet into an expanding envelope (or halo) is fundamentally diagnostic of dust ejected continuously from a discrete emission region on the sunlit side of the rotating nucleus. In a follow-up paper we will show quantitatively that, for example, the spiral jet near the nucleus on May 7 develops into the bright envelope on May 8 and 9. Dust-rich comets, such as Comet Bennett 1970 II, likewise show this type of activity (Larson and Minton 1972; Larson 1978). This also is substantially the behavior of P/Schwassmann-Wachmann 1 in its outbursts, extensively studied by Whipple (1980), except that because of this comet's large distance from the Sun the observed evolution of the features is almost entirely controlled by ejection velocity, with radiation-pressure effects dramatically diminished.

The features on the processed images are emission *boundaries* whose positions are easily measured from the computer video display with an internal movable cursor. The display facilitates positional measurement of features by allowing one to change brightness and contrast and thereby to optimize visibility. Examples of strong dust features seen in Figs. 3–6 are displayed in plots of projected distance from the nucleus, x, vs position angle, P, in Fig. 7. The slopes in the polar-coördinate diagrams measure the combined effect

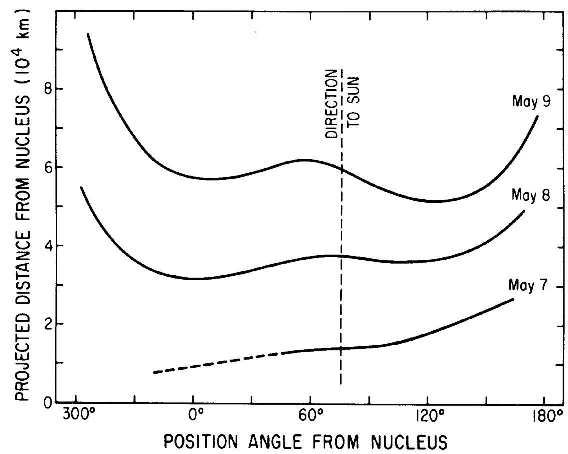

FIG. 7. Boundaries of an expanding dust feature in Comet Halley on May 7–9, 1910, depicted in a plot of the projected distance from the nucleus vs position angle. The dashed portion of the May 7 curve refers to the inner coma, where the feature's boundary is poorly defined.

of the projected particle velocities and projected nucleus spin rate. From the identification of the features on consecutive nights we find that the projected velocities show a distinct asymmetry relative to the radius vector (Fig. 7) and vary characteristically from 0.2 to 0.3 km/s, as measured in the general direction of the Sun. At the given heliocentric distances these velocities are by a factor of more than 2 lower than the halo expansion velocities of 27 comets studied by Bobrovnikoff (1954) would indicate. This velocity range also applies to the bright, nearly circular feature visible on the June 3–4 images. Probably the product of a major outburst, this halo could be related to the conspicuous cigar-shaped feature which is projecting in the antisunward direction and moves away from the nucleus at a comparably low velocity.

Analysis of plasma structures is complicated by the presence of the dust features. Nevertheless, ion rays are easily identified on a series of four exposures spanning 69 min on June 2. The plates taken on later days had longer exposures and the ion streamers were blurred by motion. For plasma-formation studies, spectrally selective imaging is essential as a means of isolating the CO^+ emissions and suppressing dust.

V. RELATIVE PHOTOMETRY OF A DUST JET

To compare the dust environment in jets with that outside them (referred to as the coma background) we undertook limited photometry of the head. Since none of the Mount Wilson plates had sensitometric calibration, we were in need of a pair of plates of different exposure times taken successively on the same night to carry out an approximate density-to-intensity conversion. The choice of plates was dictated by the presence of a well-defined jet and by a sufficiently large difference in the exposure times. Also, it was essential that a representative coma background be well established and that the projected image of the jet be free from the contamination by other overlapping features. Inspection of the plates showed that in practice these conditions are reasonably satisfied on only rare occasions.

A good opportunity to study the distribution of light in a bright jet was afforded by a pair of plates taken on May 9. The longer exposure was 8 min and the shorter 2 min. From the comparison of the densities at a number of points in the coma it was possible to build up a characteristic curve by segments over the complete range of densities. The resulting curve could be expressed as a five-coefficient modified Honeycutt-Chaldu function (Beebe 1974). This approach ignores the possible effects of reciprocity failure, changing sky conditions, and inconsistent development. However, the same procedure yielded relative intensities correct to about 10% when applied to calibrated, graduated-exposure photographs of Comet Bennett 1970 II.

The longer May 9 exposure is reproduced in Fig. 8 [Plate 17], showing the points at which the brightness was measured. The figure also presents the plots of brightness versus distance x from the nucleus in the jet and in the coma background. The contrast C (in percent) of the jet at a distance x is defined as a relative brightness increment over the background,

$$C = [(I'_{\rm jet}/I_{\rm com}) - 1] \times 100, \tag{2}$$

where $I_{\rm com}$ and $I'_{\rm jet}$ are the measured brightnesses of the coma background and the jet at the same projected distance from the nucleus. $I'_{\rm jet}$ represents in fact a sum of $I_{\rm com}$ and the intrinsic jet brightness $I_{\rm jet}$. A straightforward application of Eq. (2) to the measurements in Fig. 8 would give a contrast profile with a flat maximum of almost 30% at some 6000 km from the nucleus and with the contrast decreasing at larger distances. There is an indication of a slight decrease in the contrast near the nucleus, probably a combined effect of seeing and instrumental scattering. The emulsion is sensitive to the major molecular emissions (CN and Swan bands of C_2) as well as a broad range of the continuous spectrum. As a result, the contrast as defined above does not tell us anything about the ratio of *scattered* light in and outside the jet, the quantity most directly related to the excess dust-particle number density in the jet as compared to the average density in the coma. To deconvolve the molecular and dust components, we applied a standard model for dust and Haser's (1957) model for gas. In a notation similar to Newburn's (1981), the following expressions are obtained for the column densities of dust, n_d, and gas, n_g:

$$\begin{aligned} n_d &\propto 1/x\,, \\ n_g &\propto (1/x)\,J(x; L_p, L_r). \end{aligned} \tag{3}$$

Here x is the linear projected distance from the nucleus, L_p and L_r are the scale lengths of the parent and daughter (radical) molecules, and

$$J(x; L_p, L_r) = \int_{y_{\min}}^{y_{\max}} K_0(y)dy\,, \tag{4}$$

where $y_{\min} = x/\max(L_p, L_r)$, $y_{\max} = x/\min(L_p, L_r)$, and $K_0(y)$ is the modified Bessel function of the second kind and zero order. Since the surface brightness is proportional to the column density, the contributions from dust and from N different molecular species to a total brightness I at distance x can be expressed as

$$I(x) = \frac{1}{x}\left(W_d + \sum_{i=1}^{N} W_{g,i} J(x; L_{p,i}, L_{r,i})\right), \tag{5}$$

where the index i identifies the molecular species and W_d and $W_{g,i}$ are the weight factors of the individual contributing components. For $N = 1$ the validity of Eq. (5) can be tested graphically by plotting the product $xI(x)$ vs the integral J; the slope of the relation is given by $W_g (\equiv W_{g,1})$, whereas the ordinate at $J = 0$ is equal to W_d.

Because of the randomization of molecular motions, gas emissions from the various regions of the nucleus have a tendency to blend indiscriminately in the coma, so that the weight factors for a neutral-gas species measured in a jet, $(W_g)_{\rm jet}$, and in the coma background, $(W_g)_{\rm com}$, should essentially be the same. On the other hand, the organized motions of dust particles are diagnostic of the place of origin and the weight factors for dust, $(W_d)_{\rm jet}$ and $(W_d)_{\rm com}$, are thus measures of the dust density enhancement. In the case of a steady-state distribution the spatial density of dust varies with distance ξ from the nucleus as

$$\nu(\xi) = \nu(x)(x/\xi)^2. \tag{6}$$

Let the jet be confined to a sector AOB (Fig. 9) along the line of sight. At a fixed projected distance x the jet's column density is given by

$$[n_d(x)]_{\rm jet} = \int_{\rm (AOB)} [\nu(\xi)]_{\rm jet}\, dz = \theta_{\rm jet} x [\nu(x)]_{\rm jet}\,, \tag{7}$$

where dz is an element of length along the line of sight, $\theta_{\rm jet}$ the jet's sector angle (in radians), and $[\nu(x)]_{\rm jet}$ and $[\nu(\xi)]_{\rm jet}$ the spatial densities of dust inside the jet at the distances x and ξ, respectively. The column density along a line of sight that does not pass through the jet is related to the background spatial density of dust $[\nu(x)]_{\rm com}$ by

$$[n_d(x)]_{\rm com} = \pi x [\nu(x)]_{\rm com}\,, \tag{8}$$

whereas the jet's *apparent* column density, which also includes contributions from the coma "in front" and "behind" the jet, is

$$[n'_d(x)]_{\rm jet} = x\{\theta_{\rm jet}[\nu(x)]_{\rm jet} + (\pi - \theta_{\rm jet})[\nu(x)]_{\rm com}\}. \tag{9}$$

From Eqs. (8), (9), and (5) we find

$$\begin{aligned} \frac{[\nu(x)]_{\rm jet}}{[\nu(x)]_{\rm com}} &= 1 + \frac{\pi}{\theta_{\rm jet}}\left[\frac{(n'_d)_{\rm jet}}{(n_d)_{\rm com}} - 1\right] \\ &= 1 + \frac{\pi}{\theta_{\rm jet}}\left[\frac{(W_d)_{\rm jet}}{(W_d)_{\rm com}} - 1\right], \end{aligned} \tag{10}$$

independent of the distance x.

When applied to the brightness profiles in Fig. 8, the described approach rules out CN as the dominant molecular component, because the observed brightness decreases with distance too slowly. However, if it is assumed that the prevailing gaseous species in the photographic images is C_2, one obtains satisfactory solutions. Using Newburn and Spinrad's (1984) law for the scale length of the parent of C_2 and A'Hearn's (1982) law for the scale length of C_2 itself, we find for the May 9 plates $L_p = 2.74 \times 10^4$ km and $L_r = 6.22 \times 10^4$ km. The least-squares determined weight factors W_g and W_d for the coma background and the jet are presented, in relative units, in Table II. The "general solution" yields W_g and W_d from a two-parameter fit to Eq. (5) for $N = 1$, whereas in the "forced solution" W_d is calculated from Eq. (5) with $\langle W_g \rangle$, a weighted mean of the two values listed in columns 2 and 4, assumed. The faint portions of the jet and, especially, the coma background (at $x > 12\,000$ km) on the 2-min exposure are systematically much too bright (possibly because of the plate's uncertain fog level) and were not included in the solutions (Fig. 10). As a function of the sector angle $\theta_{\rm jet}$ the mean ratio of the spatial densities of dust in the jet and in the background coma can be estimated from the last column of Table II with the use of Eq. (10). If the jet's breadth along the

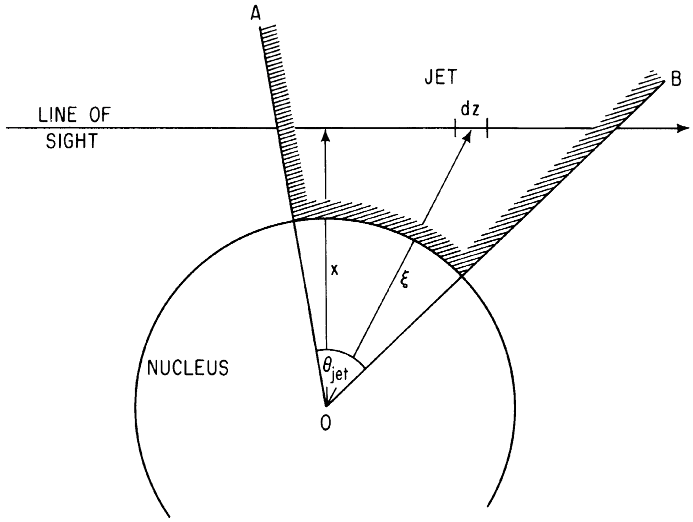

FIG. 9. Schematic illustration of the relationship between the column density and spatial density of dust particles in a jet as a function of the sector angle $\theta_{jet} = \sphericalangle AOB$ along the line of sight.

line of sight is large (say, $\theta_{jet} \simeq 90°$), the spatial density in the jet is only several times higher than in the coma. On the other hand, if the jet is relatively narrow (say, $\theta_{jet} \simeq 10°$), its spatial density may exceed that of the background by more than one order of magnitude. The surface brightness ratio of dust to C_2 along the jet in Fig. 8, calculated from the applied model, is listed for the two plates in Table III as a function of the projected distance x.

Next we briefly investigated an effect of various relative contributions from the CN emission. Extending the relation in Fig. 10, we plotted $xI(x)$ as a function of

$$J(C_2)\{1 + [J(CN)/J(C_2)][W_g(CN)/W_g(C_2)]\}$$

and found that for an assumed ratio $W_g(CN)/W_g(C_2) = 0.05$, which implies a CN/C_2 intensity ratio of 22% at a projected distance of 5000 km and 15% at 20 000 km, the resulting weight factors $(W_d)_{com}$ and $(W_d)_{jet}$ changed very little relative to those listed in Table II. A somewhat inferior, but still acceptable, fit obtained with an assumed $W_g(CN)/W_g(C_2) = 0.15$ (CN/C_2 intensity ratio between 45% and 67%) led to a jet-to-coma dust column-density ratio of ~ 10. The fit deteriorated rapidly for still higher assumed CN contributions.

Available spectra of Comet Halley, including the extensive series obtained at the Lowell Observatory (Slipher 1912; Giclas 1981), demonstrate the critical dependence of relative strengths of the emission features on the circumstances of observation (telescope, prism, plate emulsion, sky, etc.). No quantitative analysis of the CN/C_2 intensity ratio is possible from these uncalibrated spectrograms.

In the following we offer crude estimates of the four parametric functions that determine the distribution of light in the CN and C_2 emission bands on a photographic plate: (1) the energy radiated by the comet in each band; (2) the wavelength-dependent transmission of the Earth's atmosphere; (3) the spectral reflectivity of the 152-cm telescope's optics; and (4) the spectral response curve of the plate emulsion used.

No truly monochromatic fluxes of Comet Halley were measured during its 1910 apparition. Limiting our study to the 3880 Å band of CN ($B\,^2\Sigma^+ - X\,^2\Sigma^+, \Delta v = 0$) and to the three brightest Swan bands of C_2 (4740 Å, $\Delta v = +1$; 5160 Å, $\Delta v = 0$; and 5630 Å, $\Delta v = -1$), and assuming that Halley is an "average" comet in terms of the CN/C_2 abundance ratio, we used Newburn and Spinrad's (1984) results to estimate that at a heliocentric distance of the May 9 observation the CN/C_2 production-rate ratio (for the same assumed expansion velocities) should be equal to 0.18. The ratio of the total amounts of energy, E, radiated in the brightest emission bands of CN and C_2 (i.e., the ratio of their strengths) is

$$\frac{E[CN(\Delta v = 0)]}{E[C_2(\Delta v = 0)]} = \frac{Q(CN)}{Q(C_2)} \frac{L_r(CN)}{L_r(C_2)} \frac{g[CN(\Delta v = 0)]}{g[C_2(\Delta v = 0)]} = 0.88, \tag{11}$$

where Q is the production rate and g the fluorescence efficiency at 1 AU from the Sun, adopted to be 4.3×10^{-13} erg/s/radical for the CN($\Delta v = 0$) band from Tatum and Gillespie (1977) at Halley's heliocentric radial velocity of $+21$ km/s and 2.2×10^{-13} erg/s/radical for the $C_2(\Delta v = 0)$ band

TABLE II. Solutions to the brightness profiles of the coma background and the jet on two May 9, 1910 photographs (C_2 and dust).

	General solution				Forced solution			
Exposure	$(W_g)_{com}$	$(W_d)_{com}$	$(W_g)_{jet}$	$(W_d)_{jet}$	$\langle W_g \rangle$	$(W_d)_{com}$	$(W_d)_{jet}$	$\frac{(n'_d)_{jet}}{(n_d)_{com}}$
8 minutes	400	25.5	371	61.8	395.0	27.1	54.5	2.0
	± 11	± 3.2	± 23	± 7.2	...	± 3.4	± 6.4	± 0.4
2 minutes	164.0	5.5	173.5	13.8	167.4	4.6	15.3	3.3
	± 5.4	± 1.4	± 7.2	± 1.8	...	± 1.1	± 1.2	± 0.9

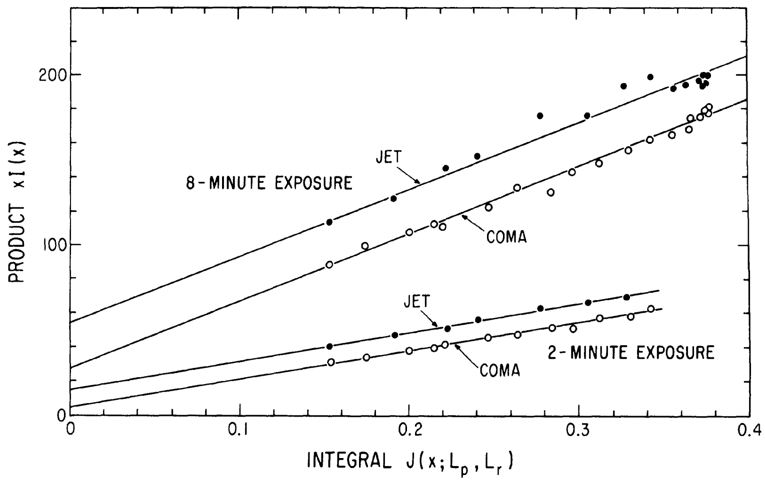

FIG. 10. Product $xI(x)$ vs integral $J(x;\, L_p,\, L_r)$ for the coma background (open symbols) and the jet (closed symbols) on the 8-min and 2-min exposures of May 9. The straight lines represent the forced solutions from Table II. The slopes give the weight factors W_g of C_2; the ordinates at $J = 0$, the weight factors W_d of dust.

from A'Hearn (1982). The relative fluxes radiated in the various Swan bands are known (A'Hearn 1978). In Table IV we present the relative strengths of the four bands of interest in the first row and the relative predicted values of the weight factors W_g^* outside the Earth's atmosphere, related to the strengths E by

$$W_g^* \propto E/|L_r - L_p|, \tag{12}$$

in the second row. The atmospheric extinction coefficients for the four effective wavelengths were interpolated from the data by Hayes and Latham (1975) for high-altitude observatories [cf. also Oke (1965) and, for early investigations, the compilation by Schoenberg (1929)] and are listed, as fractions $\eta_{\rm atm}$ of the light transmitted per unit air mass, in the third row of Table IV. On May 9 the comet's zenith angle varied from 77°.3 at the beginning of the 8-min exposure to 72°.3 at the end of the 2-min exposure. Adjusted to the altitude of the Mount Wilson Observatory above sea level, the resulting air mass from Young's (1969) formula is $\mu = 3.0 \pm 0.5$. Light losses on silver-coated mirrors are strongly wavelength dependent and increase rapidly with time as silver tarnishes markedly due to various pollutants in the air (e.g., Young and Krotkov 1929; Strong 1936; McKellar 1943). Although our efforts to find out the date of the 152-cm telescope's resilvering before the Halley observations had commenced did not meet with success, we have learned that the surfaces of both large reflectors at Mount Wilson had been reburnished about once a week and recoated once in about six months (Ingalls 1962, p. 425). Since it appears that freshly burnished silver recovers the reflecting power of a newly coated surface (Strong 1936), the reflectivity of silver mirrors a few days old, as measured by Young and Krotkov (1929), should reasonably approximate the missing data. Interestingly, Young and Krotkov commented on significant deviations between their results and the data on silver reflectivity from laboratory measurements made under environment-controlled conditions, as published in various physical tables. The adopted spectral reflectivity per mirror, $\eta_{\rm ref}$, is shown in the fourth row of Table IV. A. G. Millikan (1983, private communication) informs us that the spectral sensitivity of the (unhypersensitized) Seed 23 plates was equivalent to that of the Eastman 33 Positive, whose normalized response curve, $\eta_{\rm emu}$, is plotted in Fig. 11 and the values for the four emission bands are listed in the fifth row of Table IV. The final predicted weight factors W_g for the individual emission-band images on the May 9 plates, presented in the last row of Table IV, were calculated from the expression

$$W_g = W_g^* \eta_{\rm atm}^{\mu} \eta_{\rm ref}^2 \eta_{\rm emu}\,, \tag{13}$$

where the factor $\eta_{\rm ref}^2$ represents the light losses on the optics of the 152-cm reflector in the Newtonian configuration (two mirrors). The resulting integrated ratio of $W_g({\rm CN})/W_g(C_2) = 0.14$ implies that C_2 contributed to the photographic images about twice as much light as CN, in a reasonable agreement with our assumption.

TABLE III. Calculated surface-brightness ratio of dust to C_2 as function of projected distance along jet's image on two plates of Comet Halley taken on May 9, 1910.

Projected distance (km)	Dust-to-C_2 brightness ratio along jet on exposure: 8 minutes	2 minutes
1500	1.33	0.88
3000	0.84	0.55
5000	0.62	0.41
7500	0.50	0.33
10000	0.44	0.29
15000	0.39	0.26
20000	0.37	0.25
30000	0.37	0.25

VI. CONCLUSIONS

The application of the new radial/rotational shift-difference algorithm to the 1910 high-resolution images of P/Halley has improved considerably the visibility of coma dust and ion features. The improved contrast permits the identification of the stronger dust features over a period of up to three days. From the processed images, dust structure reveals itself as a tracer of discrete active areas emitting dust continuously from the sunlit hemisphere of the rotating nucleus. Based on measurements from the processed images, some conclusions can be drawn on the particle velocities and densities and on expectations for the 1985–1986 apparition.

A major result is the detection of expansion velocities of the envelopes in the range of 0.2–0.3 km/s. These velocities are lower than those predicted by Whipple's (1978, 1980,

TABLE IV. Predicted relative weight factors W_g for the CN and C_2 emission bands on the May 9 exposures of Comet Halley.

Emission band[a] Wavelength of head	$CN(\Delta v = 0)$ 3880 Å	$C_2(\Delta v = +1)$ 4740 Å	$C_2(\Delta v = 0)$ 5160 Å	$C_2(\Delta v = -1)$ 5630 Å	C_2(total) ...
Total energy radiated or band strength, E (relative units)	10.0	6.5	11.4	5.4	23.3
Weight factor W_g^* for intensity outside Earth's atmosphere (relative units)	10	28	49	23	100
Atmospheric transmission, η_{atm}, per unit air mass (percent)	68	81	85	87	...
Reflectivity of silver mirror, η_{ref} (percent)	57	78	81	85	...
Normalized sensitivity of plate emulsion, η_{emu} (percent)	100	60	8	$\ll 1$	...
Weight factor W_g for intensity on plate	1.0	5.4	1.6	$\ll 0.1$	7.0

[a] Adopted effective half-widths are 10 Å for the CN band and 100 Å for the C_2 bands.

1982) empirical formula (based on data compiled by Bobrovnikoff) and by Delsemme (1982) from his considerations of the interaction between gas and fine dust (0.5–0.7 km/s). In our forthcoming Paper II we will show that one can rule out the possibility that dust particles ejected from discrete emission regions achieve substantially lower terminal velocities. Such low velocities would also contradict the facts established from a detailed study of Periodic Comet Swift-Tuttle (Sekanina 1981b). Obviously, what we are measuring in Comet Halley are projected velocities along foreshortened trajectories, consistent with our concept of localized dust ejections as essentially two-dimensional structures whose initially conical surfaces are being gradually distorted by effects of radiation pressure (Sekanina and Larson 1983). At larger distances on the sunward side of the nucleus the physical deceleration of the dust by solar radiation pressure becomes increasingly evident. Our model is contrary to a traditional view which regards envelopes as projected paraboloids of isotropic emission. To avoid any misunderstanding, we emphasize that this *is not* to say that the dust ejected isotropically should not be confined to a volume about the nucleus approximately circumscribed by a paraboloid-shaped envelope as in the fountain model. Rather, this *is* to say that the *observed* envelopes have nothing in common

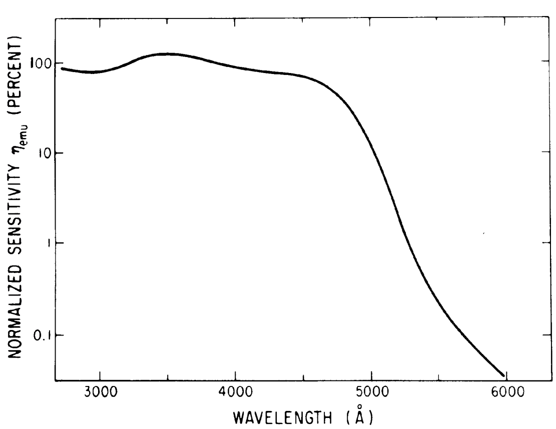

FIG. 11. Spectral response curve of the Seed 23 and Eastman 33 Positive emulsions. (Courtesy of A. G. Millikan, Eastman Kodak Research Laboratories.)

with isotropic emission and the fountain model. Indeed, the unacceptably large differences between the properties of Halley's envelopes and the predicted properties for the paraboloid envelopes (especially the deviations from the expected 2:1 ratio of the semilatus rectum to the vertex distance), discussed by Bobrovnikoff (1931), provide sufficient evidence to dismiss the traditional approach.

The nucleus rotation is documented best by the omnipresent spiral jets, clearly extending to projected distances of at least 15 000–20 000 km from the nucleus. Even with a conservative upper limit of 0.4 km/s to the "initial" projected expansion velocity, we find ~ 1 day as a *crude lower* limit to the rotation period of P/Halley, more than twice as long as Whipple's (1982) value.

Temporal changes in the dust-coma morphology may preclude the unambiguous identification of the same features when recorded at a single observatory on successive nights, but the nightly observing window is usually too short to detect motions with any degree of accuracy. Although the time scale of dust-feature changes in P/Halley somewhat relaxes the sample-frequency requirement for temporal identification from the ground, precision determinations of ejection velocities and radiation-pressure accelerations still require a baseline rate of several high-resolution images per day. This is a primary goal of the Near-Nucleus Studies Network (NNSN) of the International Halley Watch (IHW) during the 1985–1986 apparition.

The highest feature contrast directly measured on the May 9 photographs of P/Halley is about 30%, but a deconvolution of the dust and gas components leads to a jet-to-coma contrast of 100% or more in the continuum and to particle number densities in a bright jet from several to several tens of times the background density in the coma at the same distance from the nucleus. In 1986 these jets should be recorded by spacecraft imaging experiments all the way to the nucleus. Quantitative studies by Hellmich and Keller (1981) show that visibility of the nucleus is highly dependent upon particle and nucleus-surface albedos and upon the dust's optical depth. High particle concentrations in jets could substantially reduce the contrast and visibility of the nucleus, or portions thereof, as seen from spacecraft. The measured optical contrast also implies that dust detectors on spacecraft may be exposed to highly erratic particle-impact rate variations (cf. Sekanina 1983).

The prospects for visibility of coma features from the ground are good during limited periods of time in 1985–

1986. Both the pre- and post-perihelion approaches to the Earth offer extended observing windows to make continual observations of the type of features described here. We are confident that information on near-nucleus phenomena and, particularly, on nucleus-surface processes provided by the successful operation of the IHW's NNSN will be both qualitatively and quantitatively superior to the best 1910 data. In the meantime, we hope to gain an insight into the rotational and morphological properties of Halley's nucleus by analyzing carefully the currently available data. Paper II will present the first results of our quantitative study of individual dust features.

We thank G. W. Preston and B. Katem, Mount Wilson and Las Campanas Observatories, for providing access to the Halley plates taken by G. W. Ritchey with the 152-cm reflector at Mount Wilson; the Kitt Peak National Observatory directorate and E. Carder for use of the PDS microdensitometer; D. K. Yeomans, Jet Propulsion Laboratory, for supplying sets of the elements from the comet's updated orbit for the requested osculating epochs; J. Bedke and B. Katem, Mount Wilson and Las Campanas Observatories, A. G. Millikan, Eastman Kodak Research Laboratories, and R. L. Newburn, Jet Propulsion Laboratory, for their kind assistance in various aspects of our search for information on Dr. Ritchey's instrumental and photographic equipment; and especially J. S. Gotobed, Lunar and Planetary Laboratory, for implementing the new image-processing algorithm on the Space Telescope's VAX 11/780 computer at KPNO. The research described in this paper was carried out jointly by the Lunar and Planetary Laboratory, University of Arizona, and the Jet Propulsion Laboratory, California Institute of Technology, under contract with the National Aeronautics and Space Administration.

REFERENCES

A'Hearn, M. F. (1978). Astrophys. J. **219**, 768.

A'Hearn, M. F. (1982). In *Comets*, edited by L. L. Wilkening (University of Arizona, Tucson), p. 433.

Beebe, R. (1974). In *Planets, Stars, and Nebulae Studied With Photopolarimetry*, edited by T. Gehrels (University of Arizona, Tucson), p. 218.

Bobrovnikoff, N. T. (1931). Publ. Lick Obs. **17**, 305.

Bobrovnikoff, N. T. (1954). Astron. J. **59**, 357.

Comstock, G. C., Barnard, E. E., Frost, E. B., and Pickering, E. C. (1915). Publ. Astron. Astrophys. Soc. Am. **2**, 177.

Delsemme, A. H. (1982). In *Comets*, edited by L. L. Wilkening (University of Arizona, Tucson), p. 85.

Giclas, H. L. (1981). In *Modern Observational Techniques for Comets*, JPL Publ. 81-68, edited by J. C. Brandt, B. Donn, J. M. Greenberg, and J. Rahe (U.S. GPO, Washington, D.C.), p. 202.

Haser, L. (1957). Bull. Acad. R. Sci. Belg. **43**, 740.

Hayes, D. S., and Latham, D. W. (1975). Astrophys. J. **197**, 593.

Hellmich, R., and Keller, H. U. (1981). In *The Comet Halley Dust & Gas Environment*, ESA SP-174, edited by B. Battrick and E. Swallow (ESTEC, Noordwijk, The Netherlands), p. 41.

Ingalls, A. G. (1962). In *Amateur Telescope Making* (*Book One*), edited by A. G. Ingalls (Scientific American, New York), Part XI, p. 278.

Klinglesmith, D. A. (1981). In *Modern Observational Techniques for Comets*, JPL Publ. 81-68, edited by J. C. Brandt, B. Donn, J. M. Greenberg, and J. Rahe (U.S. GPO, Washington, D.C.), p. 223.

Larson, S. M. (1978). Bull. Am. Astron. Soc. **10**, 589.

Larson, S. M., and Minton, R. B. (1972). In *Comets: Scientific Data and Missions*, edited by G. P. Kuiper and E. Roemer (University of Arizona, Tucson), p. 183.

Matuska, W., Jr., Janney, D. H., Farrell, J. A., and Keller, C. F., Jr. (1978). Opt. Eng. **17**, 661.

McKellar, A. (1943). Sky Telesc. **2**, No. 8, p. 8.

Newburn, R. L. (1981). In *The Comet Halley Dust & Gas Environment*, ESA SP-174, edited by B. Battrick and E. Swallow (ESTEC, Noordwijk, The Netherlands), p. 3.

Newburn, R. L., and Spinrad, H. (1984). Astron. J. **89**, 289.

Oke, J. B. (1965). Annu. Rev. Astron. Astrophys. **3**, 23.

Rahe, J., Donn, B., and Wurm, K. (1969). *Atlas of Cometary Forms*, NASA SP-198 (U.S. GPO, Washington, D.C.), 128 pp.

Schoenberg, E. (1929). In *Handbuch der Astrophysik* (*Volume II*), edited by G. Eberhard, A. Kohlschütter, and H. Ludendorff (Springer, Berlin), p. 171.

Sekanina, Z. (1979). Icarus **37**, 420.

Sekanina, Z. (1981a). Annu. Rev. Earth Planet. Sci. **9**, 113.

Sekanina, Z. (1981b). Astron. J. **86**, 1741.

Sekanina, Z. (1983). Adv. Space Res. **2**, No. 12, p. 121.

Sekanina, Z., and Farrell, J. A. (1978). Astron. J. **83**, 1675.

Sekanina, Z., and Larson, S. M. (1983). Bull. Am. Astron. Soc. **15**, 651.

Slipher, V. M. (1912). Lowell Obs. Bull. **2**, 3.

Strong, J. (1936). Astrophys. J. **83**, 401.

Tatum, J. B., and Gillespie, M. I. (1977). Astrophys. J. **218**, 569.

Whipple, F. L. (1978). Nature **273**, 134.

Whipple, F. L. (1980). Astron. J. **85**, 305.

Whipple, F. L. (1982). In *Comets*, edited by L. L. Wilkening (University of Arizona, Tucson), p. 227.

Wood, H. J., and Albrecht, R. (1981). In *Modern Observational Techniques for Comets*, JPL Publ. 81-68, edited by J. C. Brandt, B. Donn, J. M. Greenberg, and J. Rahe (U.S. GPO, Washington, D.C.), p. 216.

Young, A. T. (1969). Icarus **11**, 1.

Young, R. K., and Krotkov, V. (1929). J. R. Astron. Soc. Can. **23**, 399.

1984AJ.....89..571L

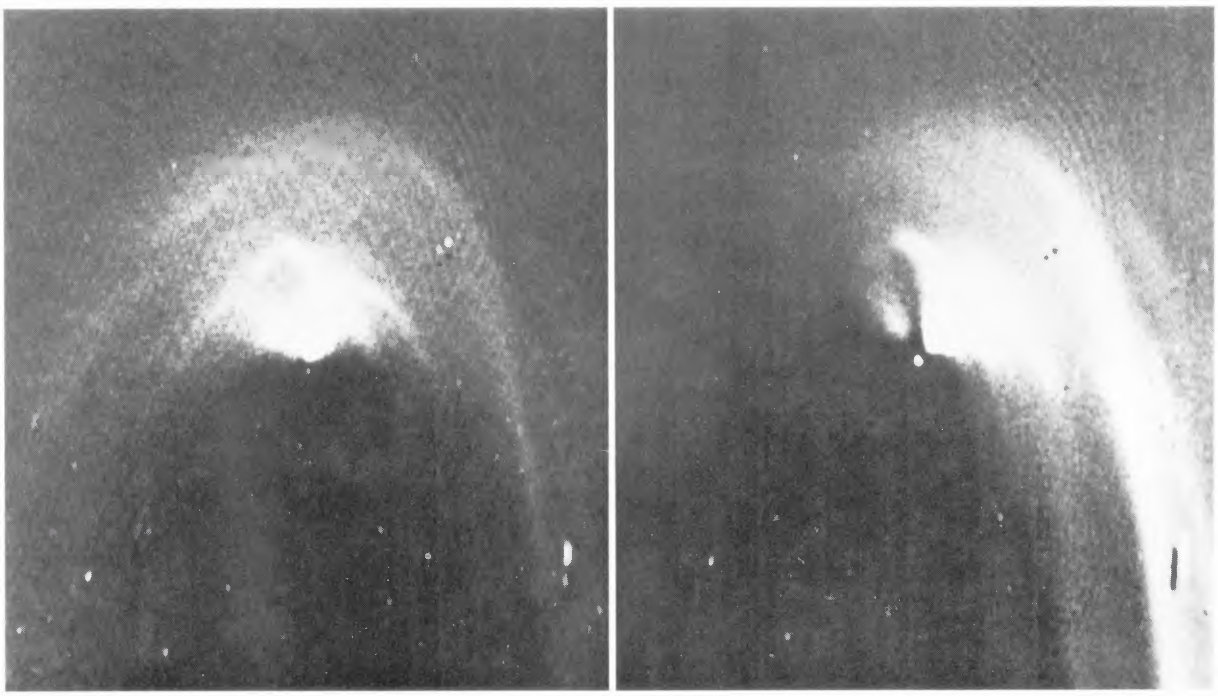

FIG. 1. Digitally processed May 9, 1910, image of Comet Halley. A linear density derivative is applied in the vertical direction (left) and in the diagonal direction (right), showing dramatic changes in the visibility of features. The ripple-like patterns in the sky background are artifacts of the scanning process.

S. M. Larson and Z. Sekanina (see page 572)

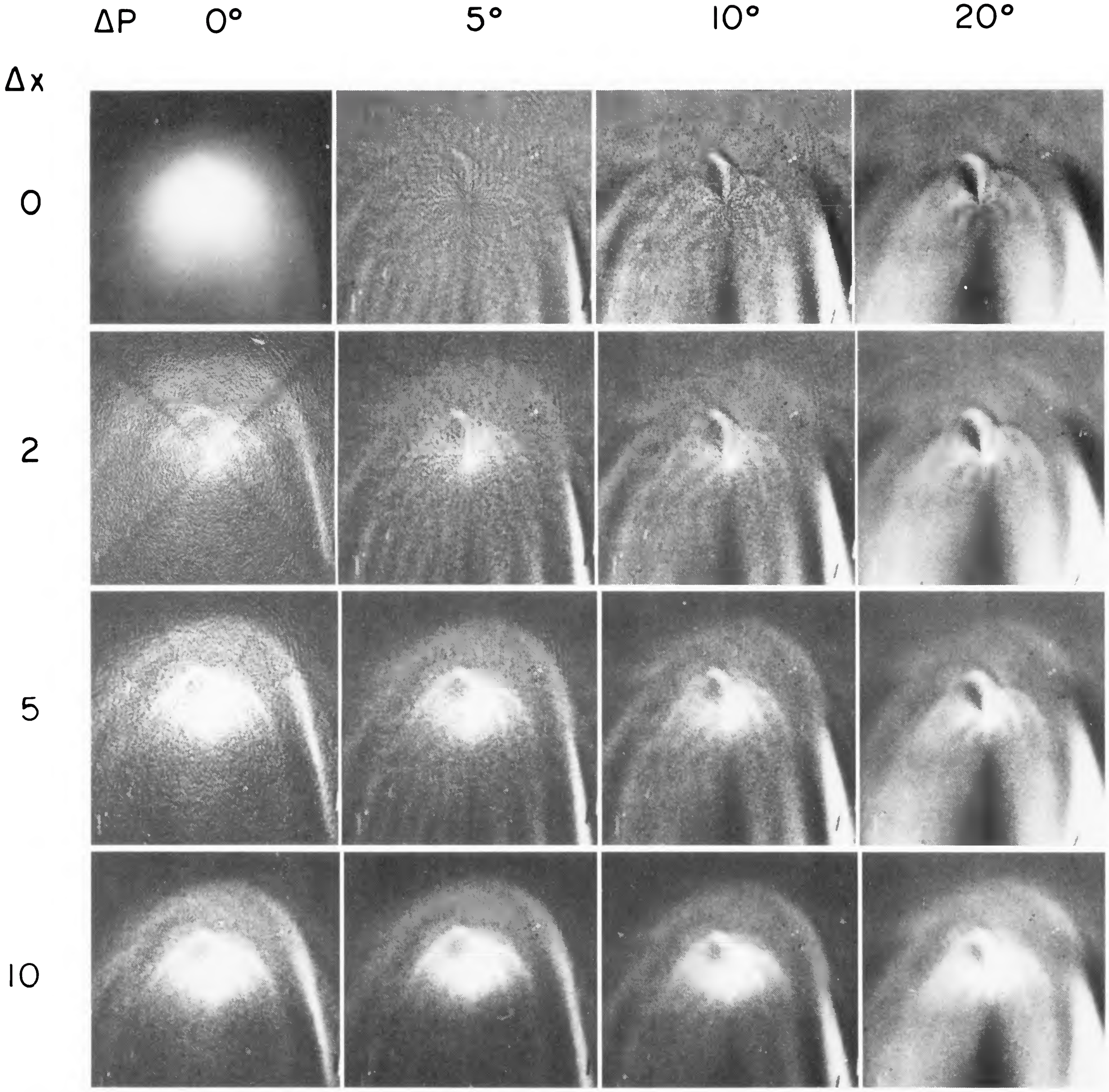

FIG. 2. Digitally processed May 9, 1910, image of Comet Halley, using the algorithm from Eq. (1). The rows exhibit the effects of constant radial shifts Δx (in pixels) and varying rotational shifts ΔP (in deg). The columns display the effects of constant ΔP and varying Δx. The unprocessed image is reproduced at $\Delta x = 0$, $\Delta P = 0°$. The radial patterns in the images $\Delta P = 0°$ and $\Delta x = 2$ and 5 pixels result from imperfect pixel interpolation. Note an improvement in the signal-to-noise ratio for larger shifts.

S. M. Larson and Z. Sekanina (see page 572)

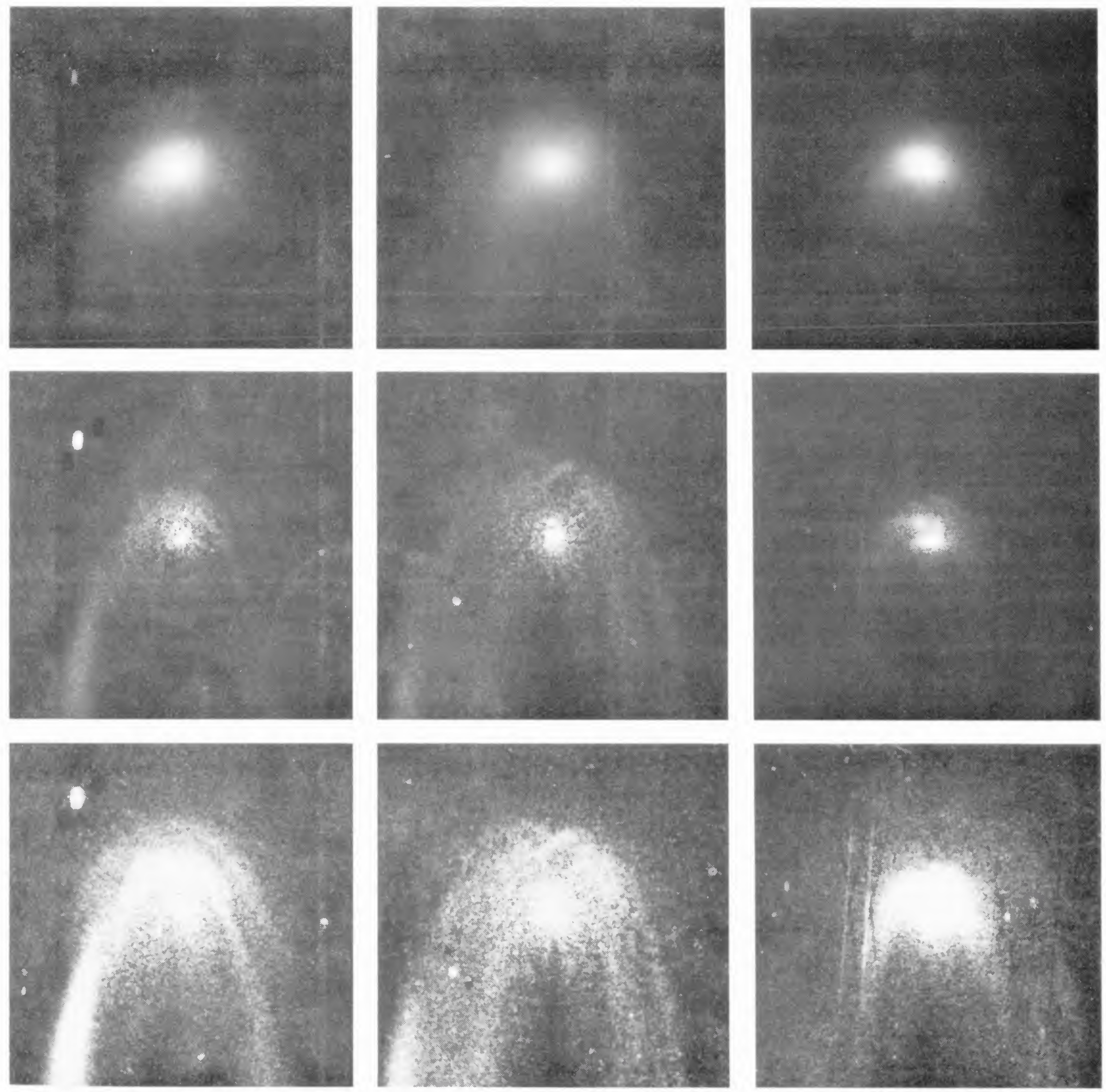

FIG. 3. Photographic observations of Comet Halley made at Mount Wilson in 1910. The times of observation are, from left to right: May 5.4900, 6.4827, and 7.4931 UT. The original images are in the top row, whereas the middle and bottom rows exhibit the digitally processed images, reproduced at two different display contrasts. The images are oriented with the Sun at the top and have a common linear scale, each frame being 180 000 km a side.

S. M. Larson and Z. Sekanina (see page 573)

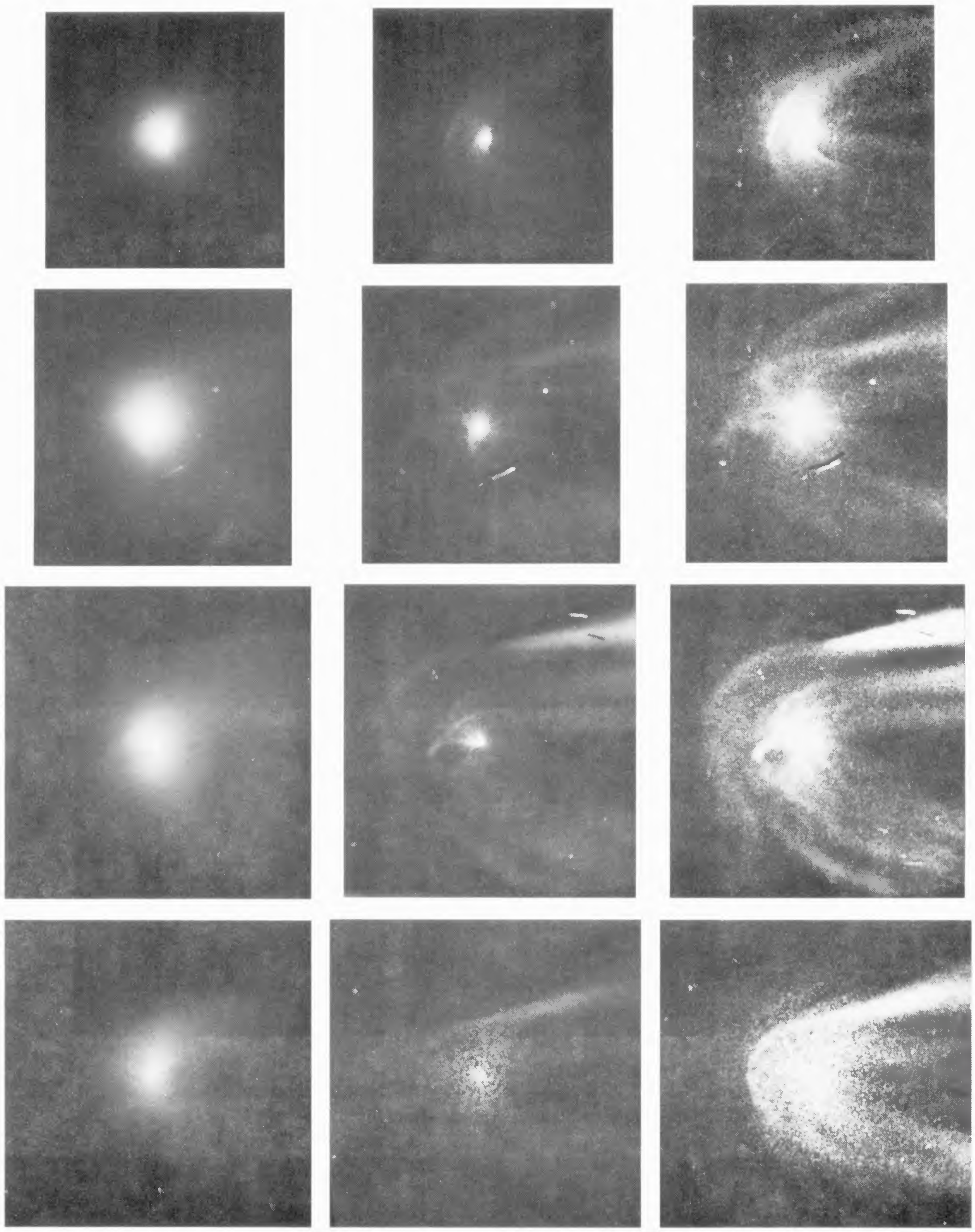

FIG. 4. Photographic observations of Comet Halley made at Mount Wilson in 1910. The times of observation are, from left to right: May 8.4885, 9.4875, 10.4938, and 11.4932 UT. The images have a common linear scale, the May 8 frame being 180 000 km a side. For other description, see the caption to Fig. 3.

S. M. Larson and Z. Sekanina (see page 573)

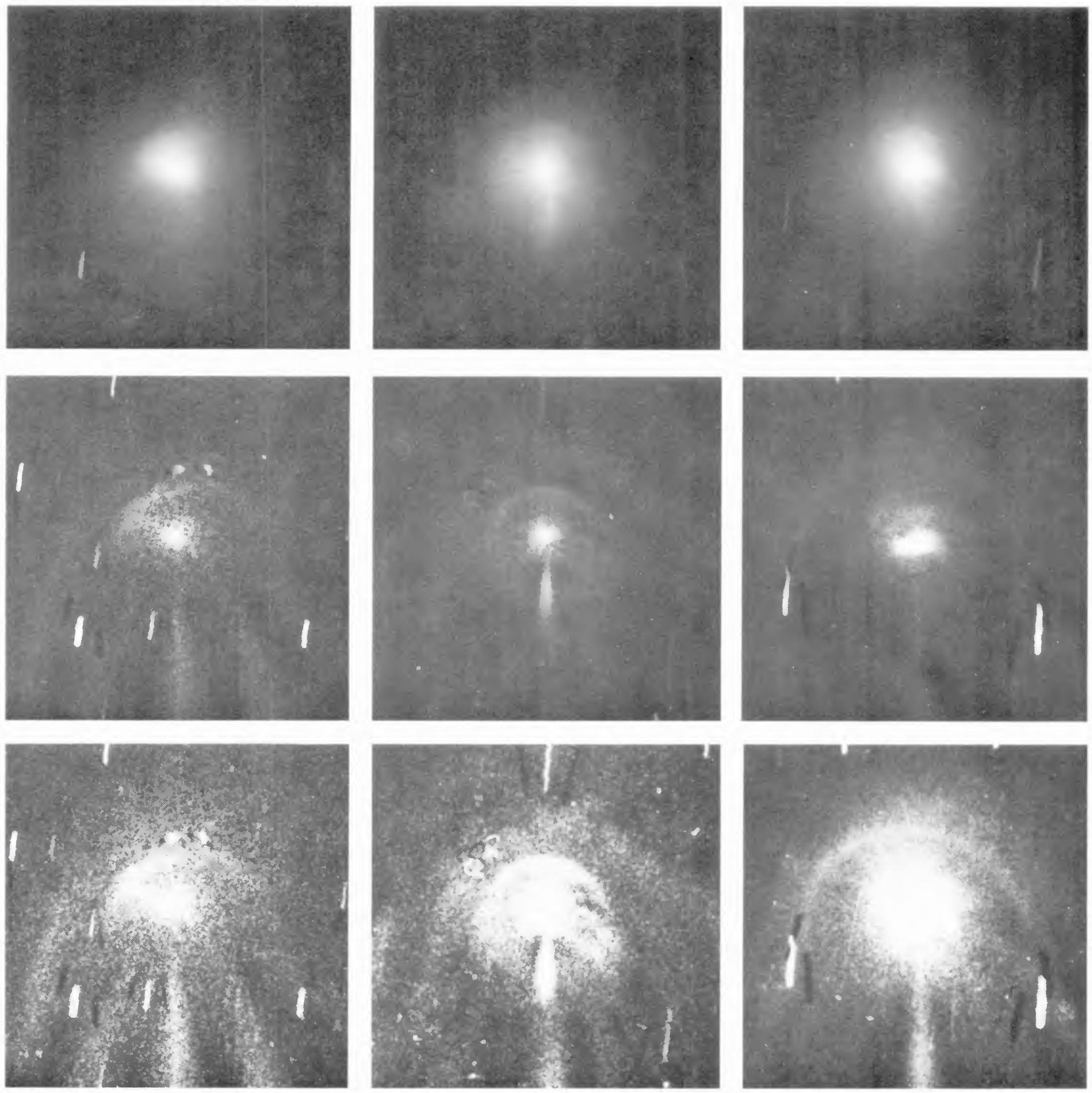

FIG. 5. Photographic observations of Comet Halley made at Mount Wilson in 1910. The times of observation are, from left to right: June 2.1815, 3.2288, and 4.2246 UT. For other description, see the caption to Fig. 3.

S. M. Larson and Z. Sekanina (see page 573)

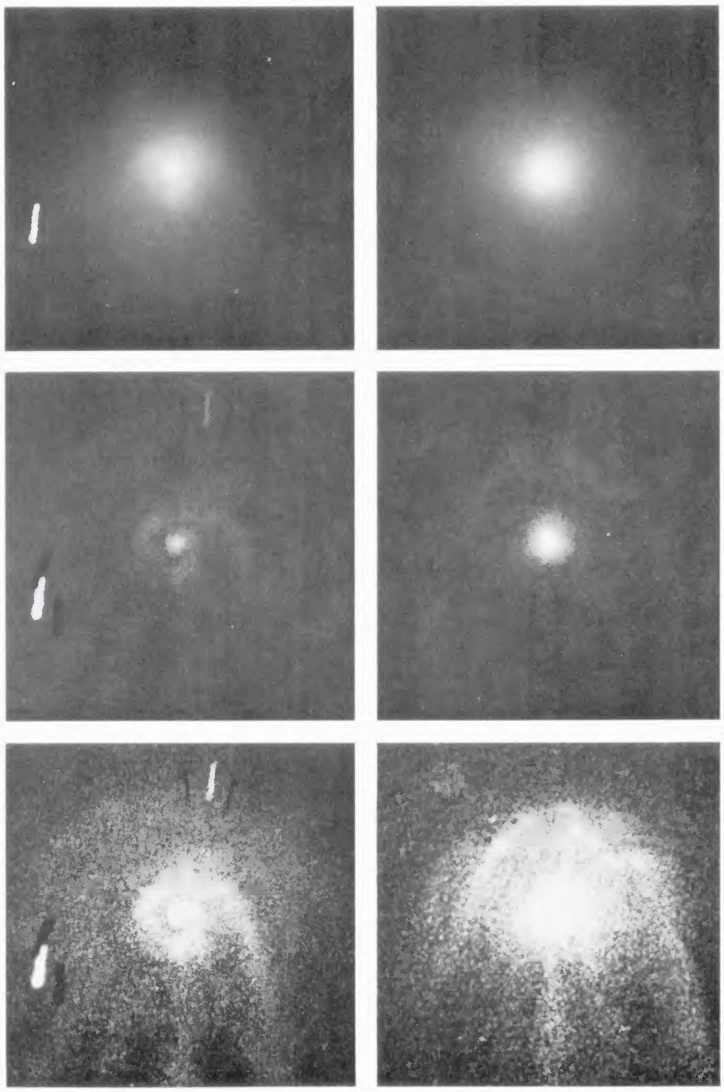

FIG. 6. Photographic observations of Comet Halley made at Mount Wilson in 1910. The time of observation is June 5.2367 for the left image, 6.2175 UT for the right. For other description, see the caption to Fig. 3.

S. M. Larson and Z. Sekanina (see page 573)

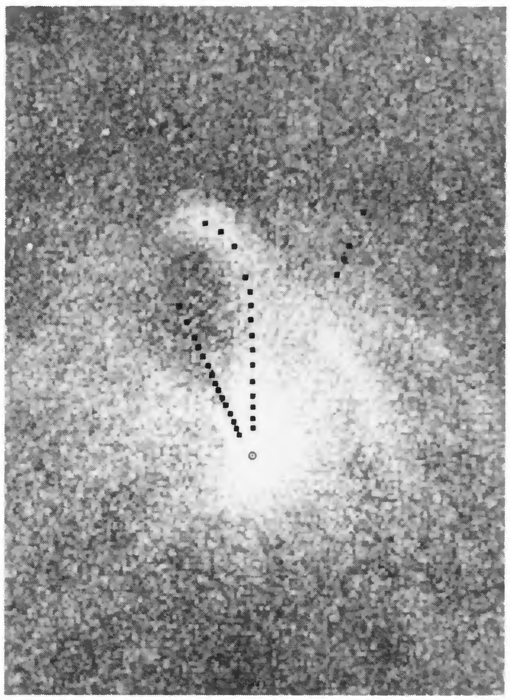

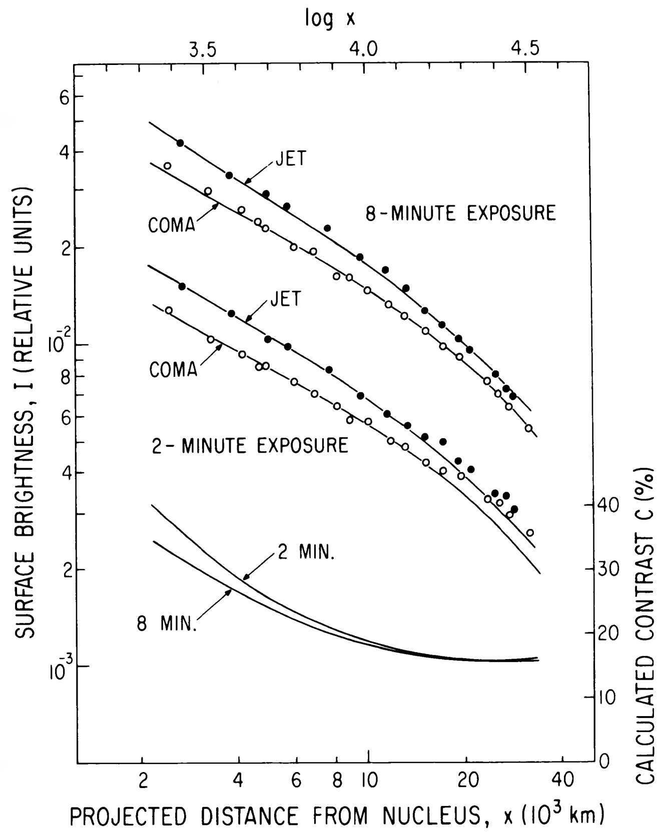

FIG. 8. *Left*: Digitized image of Comet Halley on the 8-min exposure taken on 1910 May 9 at Mount Wilson. The width of the frame is 60 000 km and the direction to the Sun is up. The approximate positions at which the brightness was measured in the coma background and in the jet are indicated by the dark marks. *Right, top*: Profiles of the coma background and the jet on the 8-min and 2-min exposures of May 9. The measured relative surface brightnesses (left scale) of the coma background (open symbols) and of the jet (closed symbols) are plotted vs projected distance from the nucleus. The curves are the forced solutions from Table II. *Right, bottom*: Jet's calculated contrast (right scale) relative to the coma background, as defined by Eq. (2), vs projected distance from the nucleus for the two exposures.

S. M. Larson and Z. Sekanina (see page 574)

THE ASTRONOMICAL JOURNAL

FOUNDED BY B. A. GOULD
1849

VOLUME 89 April 1984 ~ No. 1539 NUMBER 4

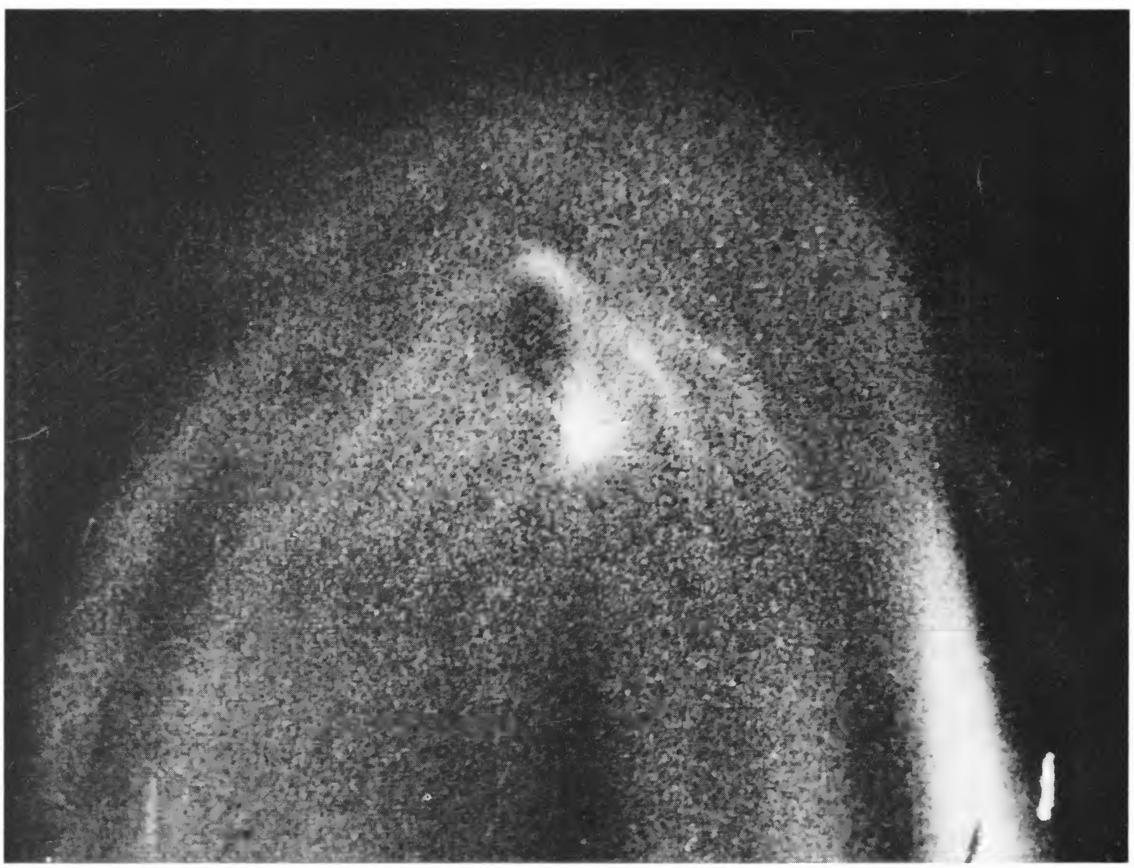

(See Page 571)

Published for the
AMERICAN ASTRONOMICAL SOCIETY
by the
AMERICAN INSTITUTE OF PHYSICS